

Intracavity spatiotemporal metasurfaces

Wenhe Jia,^{a,†} Chenxin Gao,^{a,†} Yongmin Zhao,^b Liu Li,^a Shun Wen,^a Shuai Wang,^a Chengying Bao^{✉,a,*}
Chunping Jiang,^{b,*} Changxi Yang,^a and Yuanmu Yang^{a,*}

^aTsinghua University, State Key Laboratory of Precision Measurement Technology and Instruments, Department of Precision Instrument, Beijing, China

^bChinese Academy of Sciences, Suzhou Institute of Nano-Tech and Nano-Bionics, Key Laboratory of Nanodevices and Applications, Suzhou, China

Abstract. Optical metasurfaces are endowed with unparalleled flexibility to manipulate the light field with a subwavelength spatial resolution. Coupling metasurfaces to materials with strong optical nonlinearity may allow ultrafast spatiotemporal light field modulation. However, most metasurfaces demonstrated thus far are linear devices. Here, we experimentally demonstrate simultaneous spatiotemporal laser mode control using a single-layer plasmonic metasurface strongly coupled to an epsilon-near-zero (ENZ) material within a fiber laser cavity. While the geometric phase of the metasurface is utilized to convert the laser's transverse mode from a Gaussian beam to a vortex beam carrying orbital angular momentum, the giant nonlinear saturable absorption of the ENZ material enables pulsed laser generation via the *Q*-switching process. The direct integration of a spatiotemporal metasurface in a laser cavity may pave the way for the development of miniaturized laser sources with tailored spatial and temporal profiles, which can be useful for numerous applications, such as superresolution imaging, high-density optical storage, and three-dimensional laser lithography.

Keywords: spatiotemporal control; metasurface; epsilon-near-zero; strong coupling.

Received Oct. 17, 2022; revised manuscript received Dec. 5, 2022; accepted for publication Jan. 13, 2023; published online Feb. 22, 2023.

© The Authors. Published by SPIE and CLP under a Creative Commons Attribution 4.0 International License. Distribution or reproduction of this work in whole or in part requires full attribution of the original publication, including its DOI.

[DOI: [10.1117/1.AP.5.2.026002](https://doi.org/10.1117/1.AP.5.2.026002)]

1 Introduction

The optical metasurface is an emerging class of diffractive optical elements composed of an array of dielectric or metallic nano-antennas of spatially varying geometries. It is extremely versatile for maneuvering the amplitude, phase, or polarization of incident light with a subwavelength spatial resolution.^{1–4} Over the last decade, metasurfaces have been proposed for various applications ranging from imaging^{5,6} and holography^{7–9} to the generation of complex vectorial light field patterns.^{10–14} However, most optical metasurfaces demonstrated to date are isolated optical elements that work with external light sources. Recent work indicates that the incorporation of metasurface in a solid-state or fiber laser cavity may enable coherent light emission with tailored spatial mode profile, such as vortex laser beam carrying orbital angular momentum (OAM), in a compact form factor.^{15–17} The integration of metasurface into a laser

cavity may pave the way for the development of the next generation of miniaturized laser sources with a tailorable structured light field.¹⁸

However, despite their versatility to spatially manipulate the light field, most metasurfaces only possess a time-invariant response postfabrication. Recently, there has been a growing interest in the community to develop nonlinear metasurfaces for spatiotemporal light-field modulation.¹⁹ Introducing temporal modulation to metasurfaces may unlock a much wider range of applications. For instance, all-optical switching of metasurfaces may be further utilized for saturable absorption²⁰ and temporal laser pulse shaping²¹ by leveraging the optical nonlinearity of the composite material. Nonetheless, regardless of the enhancement of nonlinear light–matter interaction in metasurfaces, most materials, either dielectric or metallic, have a relatively limited nonlinear optical response on their own, resulting in a small modulation depth and a large pump fluence requirement of nonlinear metasurfaces.

One solution to the metasurface's limited nonlinearity is through near-field coupling to a medium with extremely large optical nonlinearity. Epsilon-near-zero (ENZ) materials, an

*Address all correspondence to Yuanmu Yang, ymyang@tsinghua.edu.cn; Chunping Jiang, cpjiang2008@sinano.ac.cn; Chengying Bao, cbao@tsinghua.edu.cn

[†]These authors contributed equally to this work.

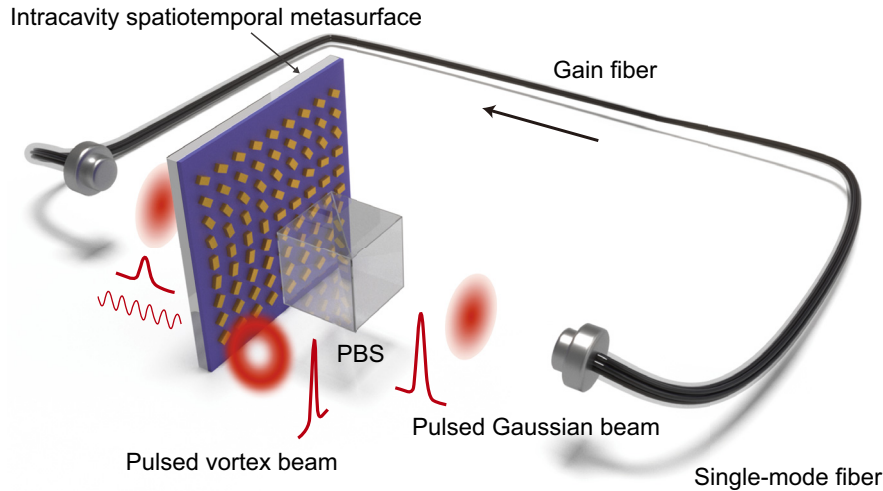


Fig. 1 Schematic illustration of the intracavity spatiotemporal modulation using the geometric phase metasurface strongly coupled to an epsilon-near-zero material. The metasurface is incorporated in a unidirectional ring fiber laser cavity. The metasurface converts a portion of the input Gaussian beam into a vortex beam, which is coupled out from the laser cavity through a polarization beam splitter (PBS). The remaining Gaussian beam is further amplified in the following round trip. The giant nonlinear saturable absorption of the strongly coupled system further allows temporal laser pulse compression via the *Q*-switching process.

emerging class of materials with vanishing permittivity, have drawn much attention in recent years.^{22–25} An ENZ response may be found in various material systems, including polar dielectrics,²⁶ doped semiconductors,²⁷ metal nitrides,²⁸ and conductive metal oxides.²⁹ For instance, indium tin oxide (ITO), a conductive metal oxide widely used as transparent electrodes in solar cells and consumer electronics, typically has its real part of permittivity crossing zero in the near-infrared regime.³⁰ An ENZ material, with its linear refractive index n_0 also approaching zero, is endowed with a large nonlinear refractive index n_2 and a large nonlinear absorption coefficient β following the relation,^{31,32}

$$n_2 = \frac{3}{4\text{Re}(n_0)n_0\epsilon_0c}\chi^{(3)}, \quad (1)$$

$$\beta = \frac{2\omega}{c}\text{Im}(n_2), \quad (2)$$

where ϵ_0 is the vacuum permittivity, c is the speed of light in vacuum, ω is the angular frequency of light, and $\chi^{(3)}$ is the material's third-order nonlinear susceptibility. The giant optical nonlinearity of ENZ materials has been exploited for second- and third-harmonic generation,^{33–35} high-harmonic generation,³⁶ terahertz wave generation,^{37,38} all-optical switching,^{39–42} and temporal pulse shaping.^{43–46} Moreover, it has been shown that the strong coupling between a plasmonic metasurface and a thin film made of an ENZ material can result in a further enhanced and tailorable nonlinear optical response.^{47,48} The synergy between a spatially inhomogeneous metasurface and an ENZ material may enable simultaneous spatiotemporal light control with unprecedented flexibility.

Here, we experimentally demonstrate the spatiotemporal light-field modulation in a fiber laser cavity using a single-layer plasmonic metasurface strongly coupled to an ENZ material.

The geometric phase of a metasurface made of spatially inhomogeneous anisotropic metallic nano-antennas is utilized to tailor the transverse mode of the output laser beam. Furthermore, the giant nonlinear saturable absorption of the coupled system allows pulsed laser generation via the *Q*-switching process. As a prototype, we realize microsecond-pulsed vortex lasers with varying topological charges, as schematically illustrated in Fig. 1.

2 Results

2.1 Intracavity Spatial Modulation

First, to implement the spatial modulation of the transverse laser mode using a metasurface directly integrated into a fiber laser cavity, we build an optical setup, as schematically shown in Fig. 2(a). The light coupled out of the fiber collimator is elliptically polarized. We use a polarizer and a quarter-wave plate to convert it to circular polarization. Here, we utilize the geometric phase of anisotropic metallic nano-antennas for the phase manipulation.^{49,50} For a nano-antenna with its long axis oriented at an angle φ with respect to the x axis, as illustrated in Fig. 2(b), when a circularly polarized plane wave impinges on the metasurface, the transmitted cross-polarized light carries an additional phase of 2φ . In contrast, the wavefront of the copolarized light remains unperturbed. As a result, the cross-polarized light can be converted to the desired spatial mode, such as vortex beams carrying OAM with varying topological charges, by judiciously tailoring the metasurface's phase profile. Another quarter-wave plate is used to convert the mode-converted beam and Gaussian beam to orthogonal linearly polarized states. The mode-converted beam is then coupled out of the laser cavity by a polarization beam splitter (PBS), while the Gaussian beam is coupled back to the fiber by the fiber collimator for further amplification. The out-coupling efficiency can be engineered by tailoring the metasurface's polarization conversion efficiency.

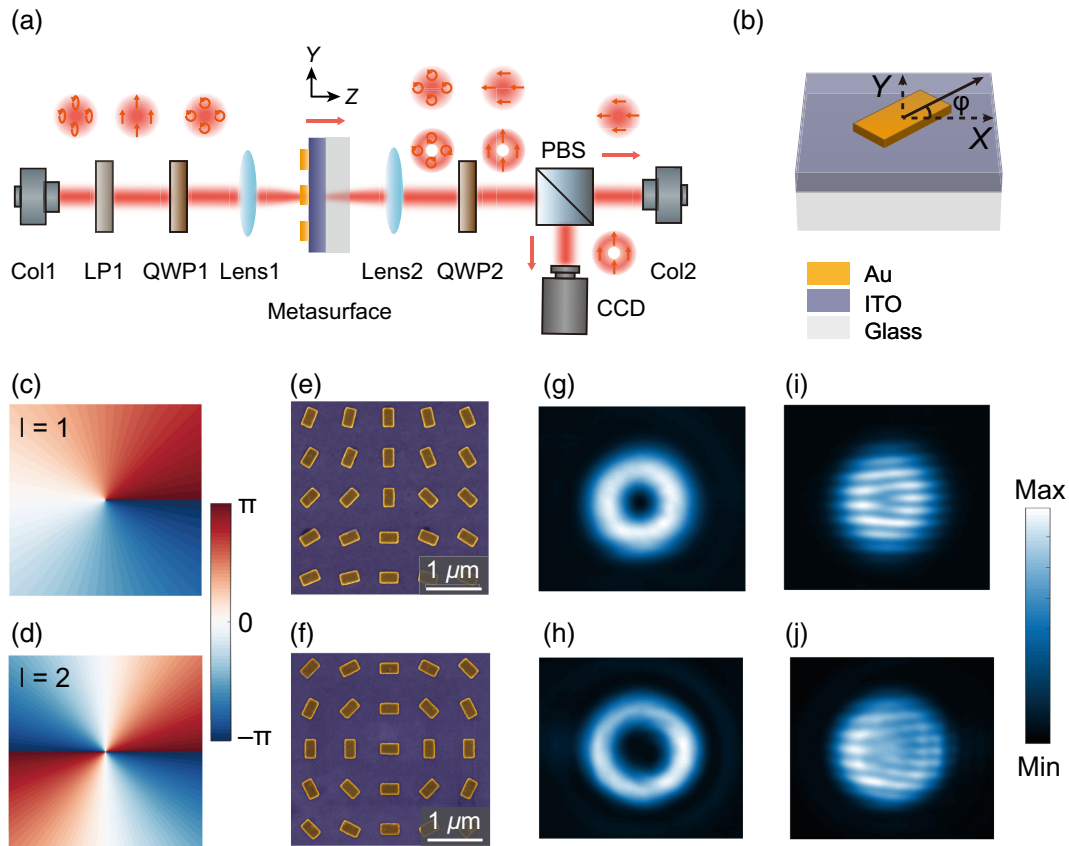


Fig. 2 Intracavity spatial modulation. (a) Schematic illustration of the optical setup in free space for the vortex beam generation using the geometric phase metasurface directly from the laser cavity. Col, collimator; LP, linear polarizer; QWP, quarter-wave plate; PBS, polarization beam splitter; CCD, charge-coupled device. (b) Schematic of the unit cell of the geometric phase metasurface. (c), (d) Spatial phase distributions required for the generation of vortex beam with topological charge $l = 1$ (c) and $l = 2$ (d), respectively. (e), (f) SEM images at the center of the geometric phase metasurface with topological charge $l = 1$ (e) and $l = 2$ (f), respectively. (g), (h) Transverse mode profiles of the vortex beam with topological charge $l = 1$ (g) and $l = 2$ (h), respectively. (i), (j) Interference patterns between a Gaussian beam and a vortex beam with topological charge $l = 1$ (i) and $l = 2$ (j), respectively.

The designed polarization conversion efficiency of the prototype metasurface, composed of gold nano-antennas on an ITO glass substrate, is merely 0.37%. Despite a relatively low polarization conversion efficiency, the remaining copolarized light experiences further stimulated amplification in the following round trip. On the contrary, most metasurfaces that operate outside of the laser cavity lack a mechanism for iteratively improving their modal conversion efficiency.

As a prototype, we experimentally demonstrate vortex fiber laser carrying OAM with topological charges $l = 1$ and $l = 2$, respectively, by incorporating the geometric phase metasurfaces in the laser cavity. The required spatial phase distributions of the cross-polarized light with $l = 1$ and $l = 2$ are illustrated in Figs. 2(c) and 2(d), respectively. The metasurfaces are fabricated by a standard single-step electron-beam lithography process, with the scanning electron microscope (SEM) images shown in Figs. 2(e) and 2(f), respectively.

The transverse mode profiles of the vortex laser beam with $l = 1$ and 2 directly coupled out from the metasurface-integrated cavity are illustrated in Figs. 2(g) and 2(h), respectively, showing a characteristic intensity minimum at the beam center,

which is a consequence of the phase singularity resulting from the corkscrew beam shape. To further confirm the topological charges of the vortex beams, we interfere each vortex beam with a Gaussian beam, with the interference patterns shown in Figs. 2(i) and 2(j), respectively (see Fig. S1 in the [Supplementary Material](#) for details). The dislocated fringe numbers in the interference patterns indicate the topological charges, which are consistent with our design.

2.2 Intracavity Temporal Modulation

Next, we investigate the nonlinear saturable absorption property when coupling the metasurface with an ENZ layer and further demonstrate temporal laser pulse shaping. Figure 3(a) shows the schematic and SEM image of a metasurface strongly coupled to an ENZ thin film made of ITO. Here, we modify the gold nano-antenna to a circular shape to rule out the competing polarization-dependent nonlinear optical effects, such as nonlinear polarization rotation,^{51–53} which could also result in temporal pulse shaping in a laser cavity.

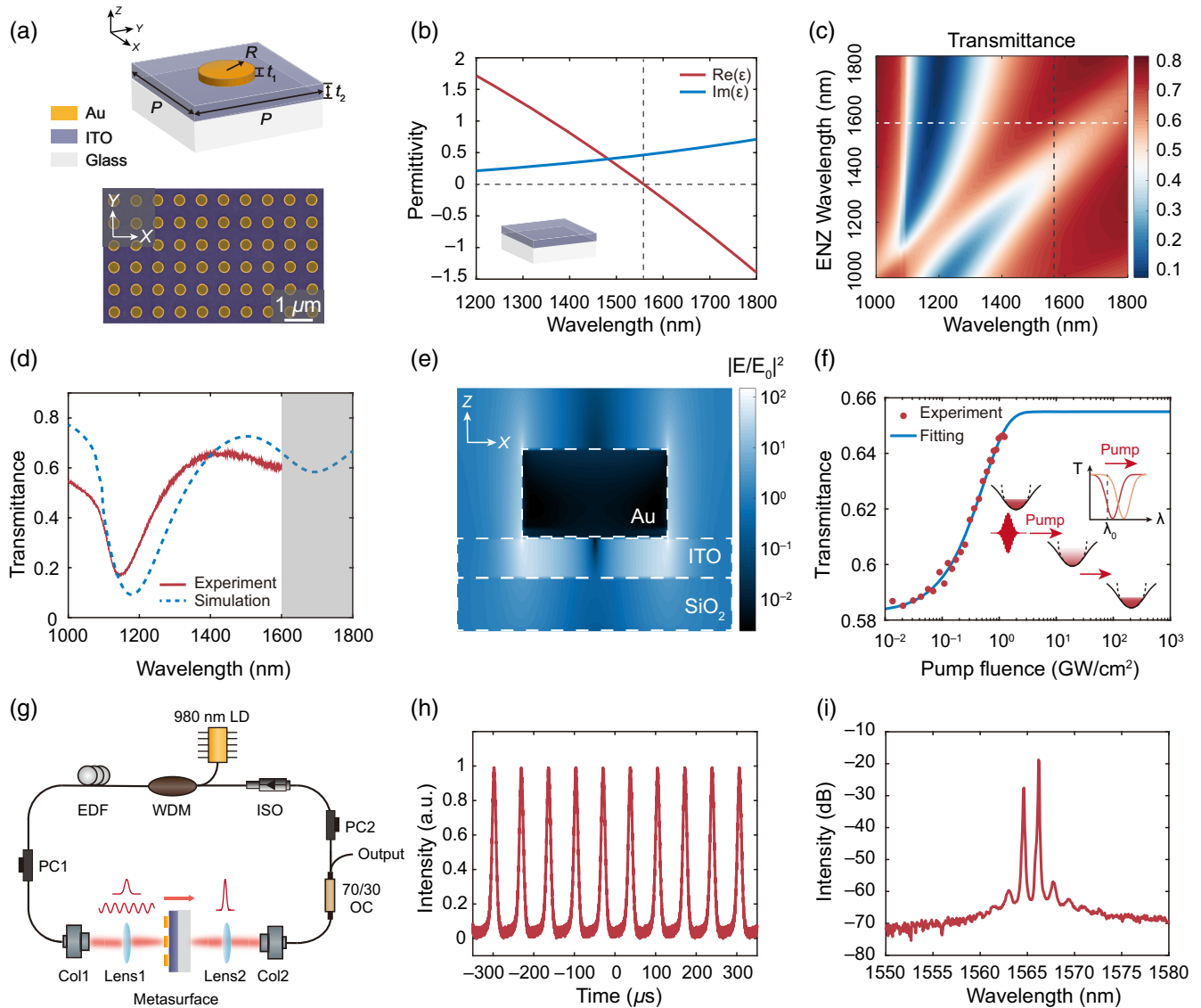


Fig. 3 Intracavity temporal modulation. (a) Schematic (upper panel) and SEM image (lower panel) of the circular gold nano-antenna coupled to an ITO film. The geometric parameters are: $P = 760\ \text{nm}$, $R = 200\ \text{nm}$, $t_1 = 40\ \text{nm}$, and $t_2 = 20\ \text{nm}$. (b) Real (red) and imaginary (blue) parts of the permittivity of the ITO film. Inset: schematic of the ITO film on glass substrate used in the spectroscopic ellipsometry measurement. (c) Simulated transmittance of the coupled system as a function of the ENZ wavelength of the ITO film. The static ENZ wavelength of the ITO film and the laser operation wavelength are indicated by the white and gray dashed lines, respectively. (d) Measured (red) and simulated (blue) linear transmittance of the coupled system. The gray region denotes the wavelength range where experimental results are not achievable due to the low quantum efficiency of the spectrometer. (e) Simulated electric field intensity distribution at the wavelength of 1565 nm. (f) Measured (dots) and fitted (line) pump fluence-dependent transmittance of the ENZ-metasurface at the wavelength of 1565 nm. The fitting parameters are as follows: $I_{\text{sat}} = 0.52\ \text{GW}/\text{cm}^2$, $A = 7.2\%$, and $A_{\text{ns}} = 34.5\%$. Inset: schematics of ultrafast electron dynamics in the ITO film with three steps, including photo-excitation, hot-electron redistribution, and relaxation. (g) Schematic of the Q-switching measurement setup. LD, laser diode; WDM, 980 nm/1550 nm wavelength division multiplexer; EDF, Er-doped fiber; ISO, optical isolator; PC, polarization controller; Col, collimator; OC, output coupler. (h) Output Q-switched pulses trace with the pump power of 39 mW. (i) Averaged optical spectrum of the output pulses with a peak wavelength of 1566 nm.

The ITO thin film is grown by magnetron sputtering, with its complex linear permittivity measured via spectroscopic ellipsometry, as shown in Fig. 3(b). The real part of its permittivity crosses zero at 1558 nm. The resonance wavelength of the gold nano-antenna is tuned to coincide with the ENZ wavelength of the ITO film. Figure 3(c) shows the simulated linear transmittance spectrum of the coupled system as a function of the ENZ wavelength of the ITO film at normal incidence, with a clear anti-crossing line shape indicating the strong coupling between the gold nano-antenna and the ITO film. The experimentally measured transmittance, as shown in Fig. 3(d), is in agreement with the simulation. The slight discrepancy is attributed to the difference of the geometry parameters of the simulated and fabricated metasurfaces as well as the inaccuracy of the fitted refractive index of the ITO film (see Fig. S2 in the [Supplementary Material](#) for details).

The simulated near-field distribution of the coupled system at a wavelength of 1565 nm is depicted in Fig. 3(e), showing over 2 orders of magnitude of enhancement of the electric field intensity within the ITO film. Despite the large third-order optical nonlinearity of a bare ENZ film that is only accessible at an oblique angle of incidence, coupling the ENZ film with the gold nano-antenna can further boost its nonlinearity at normal incidence.⁴⁷

To evaluate the nonlinear saturable absorption property of the strongly coupled system, as required for the temporal laser pulse shaping, we measure its transmittance T as a function of the pump fluence I , with the result shown in Fig. 3(f). By fitting the experimental data with the following equation:⁵⁴

$$T(I) = 1 - A \exp(-I/I_{\text{sat}}) - A_{\text{ns}}, \quad (3)$$

where I_{sat} is the saturable fluence, A is the modulation depth, and A_{ns} is the unsaturable loss, it can be determined that $I_{\text{sat}} = 0.52 \text{ GW/cm}^2$ for the metasurface strongly coupled to the ENZ layer, which is much lower than that of a bare ITO film³⁰ (see Fig. S3, Fig. S5, and Table S1 in the [Supplementary Material](#) for details).

The underlying physical mechanism for the observed saturable absorption in the ITO film is graphically depicted in the inset of Fig. 3(f). Following the subbandgap photo-excitation, the electrons in ITO's conduction band quickly thermalize into a hot Fermi distribution and relax back to the band minimum. Owing to the nonparabolicity of ITO's conduction band, its effective electron mass m_{eff} increases upon photo-excitation, leading to a redshift of ITO's ENZ wavelength and a transmittance change of the strongly coupled system.^{39,40,55} An additional advantage of the strongly coupled system is that it offers the flexibility to engineer the sign of the nonlinear refractive index by engineering either the antenna resonance or the ENZ wavelength, allowing the system to exhibit saturable or reverse-saturable absorption, depending on the application requirements.⁴⁷

To demonstrate temporal laser pulse shaping, we build an experimental setup, as schematically illustrated in Fig. 3(g). The fiber laser operates in the continuous-wave mode without the metasurface. After inserting the metasurface, a stable Q -switched pulse train is observed. The full width at half-maximum (FWHM) duration of the pulse is measured to be 11.8 μs with a pump power of 39 mW [Fig. 3(h)], and the peak wavelength is at 1566 nm [Fig. 3(i)]. The modulation with a period of 1.5 nm in the measured optical spectrum is a result of the Fabry-Perot interference in the $\sim 530\text{-}\mu\text{m}$ -thick glass substrate

that supports the metasurface device. For the Q -switched pulse generation, a higher pump power should activate the saturable absorption of the metasurface in less time, resulting in a higher pulse repetition rate. As the pump power increases, the experimentally measured pulse repetition rate increases, and the pulse duration narrows (see Fig. S7 in the [Supplementary Material](#) for details). We also investigate the slope efficiency of the laser cavity. After inserting the metasurface, the slope efficiency decreases from 6.9% to 3.8%, which is attributed to the loss induced by the metasurface. (see Fig. S8 in the [Supplementary Material](#) for details).

2.3 Intracavity Spatiotemporal Modulation

Combining transverse laser mode control and temporal pulse compression, we finally demonstrate pulsed vortex laser beam generation using a single spatiotemporal metasurface incorporated in the laser cavity. Here, the metasurface utilized is identical to the one presented in Fig. 2. Its nonlinear saturable fluence I_{sat} is measured to be 0.41 GW/cm^2 (see Figs. S4–S6 and Table S2 in the [Supplementary Material](#) for details).

To generate pulsed vortex laser beams, we increase the pump fluence by moving the metasurfaces closer to the focus of the lens. The measured transverse mode profiles of the vortex laser beam with $l = 1$ and $l = 2$ directly coupled out from the metasurface-integrated cavity are shown in Figs. 4(a) and 4(b), respectively. The decrease in the mode purity may be attributed to the decreased spot size of the incident light and the resultant distorted modulated wavefront. Furthermore, the alignment requirements for the light path become more stringent as the laser spot size decreases. The measured interference patterns between the vortex beams and the Gaussian beams, as depicted in Figs. 4(c) and 4(d), respectively, further confirm that the topological charges of the generated vortex beams agree with the theoretical prediction. With a pump power of 51 mW, the FWHM duration of the Q -switched vortex pulse is 14.3 μs [Fig. 4(e)], and the peak wavelength is at 1578 nm [Fig. 4(f)]. The pulse duration and repetition rate can be controlled by adjusting the pump power (see Fig. S9 in the [Supplementary Material](#) for details). The slope efficiencies of the laser cavity for Gaussian beam generation with and without metasurface are 5.4% and 6.7%, respectively. The slope efficiency of the Q -switched vortex pulse from the PBS is 0.32%, as a result of the relatively low polarization conversion efficiency of the geometric phase metasurface (see Fig. S10 in the [Supplementary Material](#) for details).

3 Conclusion

We have demonstrated that a single optical element, composed of a metasurface strongly coupled to an ENZ material, can be utilized to modulate light spatiotemporally within the laser cavity. As a prototype, the pulsed vortex lasers with variable topological charges have been generated.

Looking forward, we envision that one may combine the metasurface's versatility for spatial light-field manipulation with its giant and tailorable nonlinearity for generating laser beams with arbitrary spatial and temporal profiles.⁵⁶ Since ENZ materials typically have a response time on the order of hundreds of femtoseconds,^{30,39} it is also possible to generate femtosecond vortex pulses via the mode-locking process with further suppressed cavity loss and increased pump power.⁵⁷ To further reduce the cavity loss and increase the damage threshold of the metasurface, high-index dielectric antennas may be

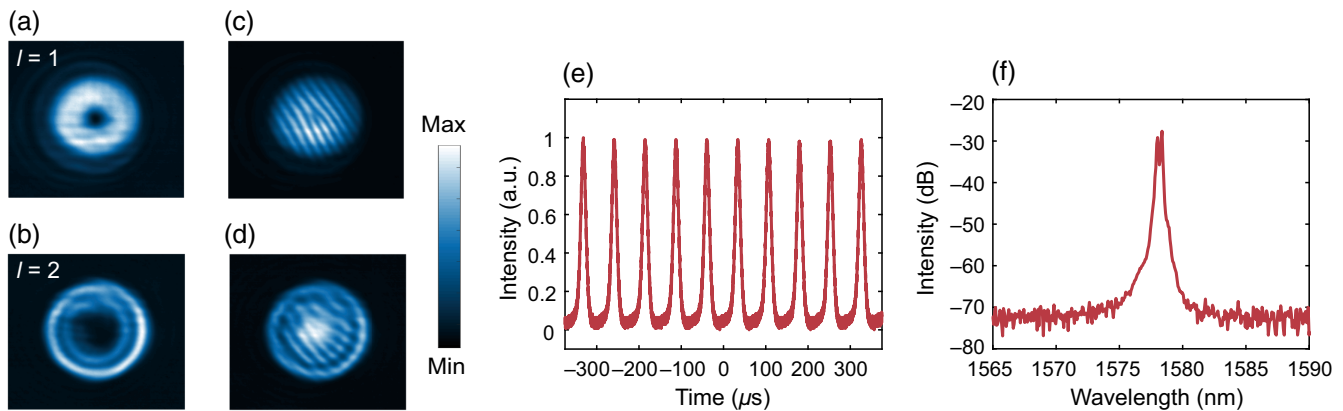


Fig. 4 Intracavity spatiotemporal modulation. (a), (b) Transverse mode profiles of the Q-switched vortex pulses with topological charge $l = 1$ (a) and $l = 2$ (b), respectively. (c), (d) Interference patterns between a pulsed Gaussian beam and a pulsed vortex beam with topological charge $l = 1$ (c) and $l = 2$ (d), respectively. (e) Q-switched pulse trace of the vortex beam ($l = 2$) with a pump power of 51 mW. The FWHM pulse duration is 14.3 μs . (f) Averaged optical spectrum of the pulsed vortex beam ($l = 2$) with a peak wavelength of 1578 nm.

used in place of metal.⁵⁸ Other nonlinear media, such as semiconductor saturable absorber mirrors, could also be incorporated into the spatiotemporal metasurface design to improve their mode-locking capabilities and broaden their operation wavelength range.⁵⁹ Furthermore, metasurfaces can be integrated on the fiber end face to avoid the coupling loss between fiber and free space and to reduce the required pump fluence. Our method may break ground for developing the next generation of miniaturized pulsed laser sources with designer transverse mode profiles, which could be used in various applications,⁶⁰ such as light trapping,⁶¹ optical storage,⁶² superresolution imaging,⁶³ and 3D laser lithography.⁶⁴

Note: See [Supplementary Material](#) for methods for metasurfaces fabrication and ITO thin-film growth, linear characteristics of the ITO film, nonlinear optical effect contribution analysis and polarization-selective effect analysis of the geometric phase metasurfaces, which includes Fig. S11 and Refs. 65 and 66.

Acknowledgments

We thank Mr. Xi Feng at Tianjin University for his help in annealing the ITO film. This work is supported by the National Natural Science Foundation of China (62135008, 61975251) and by the Guoqiang Institute, Tsinghua University. All other authors declare they have no competing interests.

Code, Data, and Materials Availability

All data needed to evaluate the conclusions in the paper are present in the paper and/or the Supplementary Materials. The software codes and the raw data that support the plots within this paper are available from the corresponding authors upon reasonable request.

References

1. A. V. Kildishev, A. Boltasseva, and V. M. Shalaev, "Planar photonics with metasurfaces," *Science* **339**(6125), 1232009 (2013).
2. P. Genevet et al., "Recent advances in planar optics: from plasmonic to dielectric metasurfaces," *Optica* **4**(1), 139–152 (2017).

3. K. Koshelev and Y. Kivshar, "Dielectric resonant metaphotonics," *ACS Photonics* **8**(1), 102–112 (2020).
4. J. Yang et al., "Active optical metasurfaces: comprehensive review on physics, mechanisms, and prospective applications," *Rep. Prog. Phys.* **85**(3), 036101 (2022).
5. X. Chen et al., "Dual-polarity plasmonic metalens for visible light," *Nat. Commun.* **3**, 1198 (2012).
6. M. Khorasaninejad et al., "Metalenses at visible wavelengths: diffraction-limited focusing and subwavelength resolution imaging," *Science* **352**(6290), 1190–1194 (2016).
7. X. Ni, A. V. Kildishev, and V. M. Shalaev, "Metasurface holograms for visible light," *Nat. Commun.* **4**, 2807 (2013).
8. L. Huang et al., "Three-dimensional optical holography using a plasmonic metasurface," *Nat. Commun.* **4**, 2808 (2013).
9. G. Zheng et al., "Metasurface holograms reaching 80% efficiency," *Nat. Nanotechnol.* **10**(4), 308–312 (2015).
10. N. Yu et al., "Light propagation with phase discontinuities: generalized laws of reflection and refraction," *Science* **334**(6054), 333–337 (2011).
11. Y. Yang et al., "Dielectric meta-reflectarray for broadband linear polarization conversion and optical vortex generation," *Nano Lett.* **14**(3), 1394–1399 (2014).
12. R. C. Devlin et al., "Arbitrary spin-to-orbital angular momentum conversion of light," *Science* **358**(6365), 896–901 (2017).
13. H. Chung et al., "E-band metasurface-based orbital angular momentum multiplexing and demultiplexing," *Laser Photonics Rev.* **16**(6), 2100456 (2022).
14. L. Chen et al., "Spatiotemporal control of femtosecond pulses," in *CLEO: Appl. and Technol.* (Optica Publishing Group, 2022), paper JTh2P.2.
15. E. Maguid et al., "Topologically controlled intracavity laser modes based on pancharatnam-berry phase," *ACS Photonics* **5**(5), 1817–1821 (2018).
16. H. Sroor et al., "High-purity orbital angular momentum states from a visible metasurface laser," *Nat. Photonics* **14**(8), 498–503 (2020).
17. L. Gui et al., "60-nm-span wavelength-tunable vortex fiber laser with intracavity plasmon metasurfaces," arXiv: 2207.05264 (2022).
18. A. Forbes, "Structured light from lasers," *Laser Photonics Rev.* **13**(11), 1900140 (2019).
19. A. M. Shaltout, V. M. Shalaev, and M. L. Brongersma, "Spatiotemporal light control with active metasurfaces," *Science* **364**(6441), eaat3100 (2019).

20. V. V. Zubuyuk et al., “Low-power absorption saturation in semiconductor metasurfaces,” *ACS Photonics* **6**(11), 2797–2806 (2019).
21. J. Wang et al., “Saturable plasmonic metasurfaces for laser mode locking,” *Light Sci. Appl.* **9**(1), 50 (2020).
22. X. Niu et al., “Epsilon-near-zero photonics: a new platform for integrated devices,” *Adv. Opt. Mater.* **6**(10), 1701292 (2018).
23. O. Reshef et al., “Nonlinear optical effects in epsilon-near-zero media,” *Nat. Rev. Mater.* **4**(8), 535–551 (2019).
24. N. Kinsey et al., “Near-zero-index materials for photonics,” *Nat. Rev. Mater.* **4**(12), 742–760 (2019).
25. J. Wu et al., “Epsilon-near-zero photonics: infinite potentials,” *Photonics Res.* **9**(8), 1616–1644 (2021).
26. J. D. Caldwell et al., “Low-loss, infrared and terahertz nanophotonics using surface phonon polaritons,” *Nanophotonics* **4**(1), 44–68 (2015).
27. F. Hu et al., “Two-plasmon spontaneous emission from a nonlocal epsilon-near-zero material,” *Commun. Phys.* **4**(1), 84 (2021).
28. X. Wen et al., “Doubly enhanced second harmonic generation through structural and epsilon-near-zero resonances in TiN nanostructures,” *ACS Photonics* **5**(6), 2087–2093 (2018).
29. G. V. Naik, V. M. Shalaev, and A. Boltasseva, “Alternative plasmonic materials: beyond gold and silver,” *Adv. Mater.* **25**(24), 3264–3294 (2013).
30. M. Z. Alam, I. De Leon, and R. W. Boyd, “Large optical nonlinearity of indium tin oxide in its epsilon-near-zero region,” *Science* **352**(6287), 795–797 (2016).
31. R. W. Boyd, *Nonlinear Optics*, Academic Press (2020).
32. R. W. Boyd, Z. Shi, and I. De Leon, “The third-order nonlinear optical susceptibility of gold,” *Opt. Commun.* **326**(1), 74–79 (2014).
33. T. S. Luk et al., “Enhanced third harmonic generation from the epsilon-near-zero modes of ultrathin films,” *Appl. Phys. Lett.* **106**(15), 151103 (2015).
34. A. Capretti et al., “Comparative study of second-harmonic generation from epsilon-near-zero indium tin oxide and titanium nitride nanolayers excited in the near-infrared spectral range,” *ACS Photonics* **2**(11), 1584–1591 (2015).
35. J. Deng et al., “Giant enhancement of second-order nonlinearity of epsilon-near-zero medium by a plasmonic metasurface,” *Nano Lett.* **20**(7), 5421–5427 (2020).
36. Y. Yang et al., “High-harmonic generation from an epsilon-near-zero material,” *Nat. Phys.* **15**(10), 1022–1026 (2019).
37. W. Jia et al., “Broadband terahertz wave generation from an epsilon-near-zero material,” *Light Sci. Appl.* **10**(1), 11 (2021).
38. Y. Lu et al., “Integrated terahertz generator-manipulators using epsilon-near-zero-hybrid nonlinear metasurfaces,” *Nano Lett.* **21**(18), 7699–7707 (2021).
39. P. Guo et al., “Ultrafast switching of tunable infrared plasmons in indium tin oxide nanorod arrays with large absolute amplitude,” *Nat. Photonics* **10**(4), 267–273 (2016).
40. Y. Yang et al., “Femtosecond optical polarization switching using a cadmium oxide-based perfect absorber,” *Nat. Photonics* **11**(6), 390–395 (2017).
41. F. Hu et al., “High-contrast optical switching using an epsilon-near-zero material coupled to a Bragg microcavity,” *Opt. Express* **27**(19), 26405–26414 (2019).
42. J. Bohn et al., “All-optical switching of an epsilon-near-zero plasmon resonance in indium tin oxide,” *Nat. Commun.* **12**, 1017 (2021).
43. Q. Guo et al., “A solution-processed ultrafast optical switch based on a nanostructured epsilon-near-zero medium,” *Adv. Mater.* **29**(27), 1700754 (2017).
44. J. Guo et al., “Indium tin oxide nanocrystals as saturable absorbers for passively Q-switched erbium-doped fiber laser,” *Opt. Mater. Express* **7**(10), 3494–3502 (2017).
45. X. Jiang et al., “Epsilon-near-zero medium for optical switches in a monolithic waveguide chip at 1.9 μm ,” *Nanophotonics* **7**(11), 1835–1843 (2018).
46. K. Y. Lau et al., “Tunable optical nonlinearity of indium tin oxide for optical switching in epsilon-near-zero region,” *Nanophotonics* **11**(18), 4209–4219 (2022).
47. M. Z. Alam et al., “Large optical nonlinearity of nanoantennas coupled to an epsilon-near-zero material,” *Nat. Photonics* **12**(2), 79–83 (2018).
48. X. Niu et al., “Polarization-selected nonlinearity transition in gold dolmens coupled to an epsilon-near-zero material,” *Nanophotonics* **9**(16), 4839–4851 (2020).
49. L. Huang et al., “Dispersionless phase discontinuities for controlling light propagation,” *Nano Lett.* **12**(11), 5750–5755 (2012).
50. E. Karimi et al., “Generating optical orbital angular momentum at visible wavelengths using a plasmonic metasurface,” *Light Sci. Appl.* **3**(5), e167 (2014).
51. V. Matsas et al., “Self-starting, passively mode-locked fibre ring soliton laser exploiting non-linear polarisation rotation,” *Electron. Lett.* **28**(15), 1391–1393 (1992).
52. Y. Ding et al., “Spatiotemporal mode-locking in lasers with large modal dispersion,” *Phys. Rev. Lett.* **126**(9), 093901 (2021).
53. K. Liu, X. Xiao, and C. Yang, “Observation of transition between multimode Q-switching and spatiotemporal mode locking,” *Photonics Res.* **9**(4), 530–534 (2021).
54. B. Fu et al., “Passively Q-switched Yb-doped all-fiber laser based on Ag nanoplates as saturable absorber,” *Nanophotonics* **9**(12), 3873–3880 (2020).
55. H. Wang et al., “Extended Drude model for intraband-transition-induced optical nonlinearity,” *Phys. Rev. Appl.* **11**(6), 064062 (2019).
56. A. Chong et al., “Generation of spatiotemporal optical vortices with controllable transverse orbital angular momentum,” *Nat. Photonics* **14**(6), 350–354 (2020).
57. C. Wei et al., “Mid-infrared Q-switched and mode-locked fiber lasers at 2.87 μm based on carbon nanotube,” *IEEE J. Sel. Top. Quantum Electron.* **25**(4), 1100206 (2019).
58. K. Wang et al., “Large optical nonlinearity of dielectric nanocavity-assisted mie resonances strongly coupled to an epsilon-near-zero mode,” *Nano Lett.* **22**(2), 702–709 (2022).
59. U. Keller et al., “Semiconductor saturable absorber mirrors (SESAM’s) for femtosecond to nanosecond pulse generation in solid state lasers,” *IEEE J. Sel. Top. Quantum Electron.* **2**(3), 435–453 (1996).
60. A. Forbes, M. de Oliveira, and M. R. Dennis, “Structured light,” *Nat. Photonics* **15**(4), 253–262 (2021).
61. M. Padgett and R. Bowman, “Tweezers with a twist,” *Nat. Photonics* **5**(6), 343–348 (2011).
62. M. Gu, X. Li, and Y. Cao, “Optical storage arrays: a perspective for future big data storage,” *Light Sci. Appl.* **3**(5), e177 (2014).
63. G. Vicidomini, P. Bianchini, and A. Diaspro, “STED super-resolved microscopy,” *Nat. Methods* **15**(3), 173–182 (2018).
64. D. D. Han et al., “Light-mediated manufacture and manipulation of actuators,” *Adv. Mater.* **28**(38), 8328–8343 (2016).
65. X. Liu et al., “Quantification and impact of nonparabolicity of the conduction band of indium tin oxide on its plasmonic properties,” *Appl. Phys. Lett.* **105**(18), 181117 (2014).
66. M. D. Tocci et al., “Thin-film nonlinear optical diode,” *Appl. Phys. Lett.* **66**(18), 2324–2326 (1995).

Wenhe Jia received his BS degree in optoelectronics from Nankai University. He is a PhD student at Tsinghua University, supervised by Prof. Yuanmu Yang. His current research focuses on the study of nonlinear optics and nanophotonics.

Chenxin Gao received her BS degree in optoelectronic information science and engineering from Wuhan University of Technology. She is a PhD student at Tsinghua University, supervised by Prof. Changxi Yang and Prof. Chengying Bao. Her current research interests are in spatiotemporal mode-locking in fiber lasers.

Chengying Bao is an assistant professor at Tsinghua University, where he received his PhD in 2016. Then he worked as a postdoc at Purdue University and Caltech. He mainly works on microresonators, optical frequency combs, integrated nonlinear optics, and ultrafast optics.

Chunping Jiang received her PhD in microelectronics and solid-state electronics from Shanghai Institute of Technical Physics, Chinese Academy of Sciences (CAS), China, in 2002. Currently, she is a professor in the Division of Nano-Devices and Related Nano-Materials, Suzhou Institute of Nano-Tech and Nano-Bionics, CAS. Her research interests include plasmonic materials, metasurfaces, and on-chip nanophotonic devices and systems.

Yuanmu Yang received his BE degree in optoelectronics from Tianjin University in 2011 and his PhD from Vanderbilt University in 2015. He is an associate professor in the Department of Precision Instruments, Tsinghua University. Before joining Tsinghua in 2018, he worked as a postdoc at Sandia National Laboratories and as a research scientist at Intellectual Ventures. His research focuses on meta-optics and its applications in miniaturized optical devices and systems.

Biographies of the other authors are not available.